Greenness indices from digital cameras predict the timing and seasonal dynamics of canopy-scale photosynthesis

Michael Toomey, Mark A. Friedl, Steve Frolking, Koen Hufkens, Stephen Klosterman, Oliver Sonnentag, Dennis D. Baldocchi, Carl J. Bernacchi, Sebastien C. Biraud, Gil Bohrer, Edward Brzostek, Sean P. Burns, Carole Coursolle, David Y. Hollinger, Hank A. Margolis, Harry McCaughey, Russell K. Monson, J. William Munger, Stephen Pallardy, Richard P. Phillips, Margaret S. Torn, Sonia Wharton, Marcelo Zeri, Andrew D. Richardson

First published: 01 January 2015
https://doi.org/10.1890/14-0005.1

Abstract

The proliferation of digital cameras co-located with eddy covariance instrumentation provides new opportunities to better understand the relationship between canopy phenology and the seasonality of canopy photosynthesis. In this paper we analyze the abilities and limitations of canopy color metrics measured by digital repeat photography to track seasonal canopy development and photosynthesis, determine phenological transition dates, and estimate intra-annual and interannual variability in canopy photosynthesis. We used 59 site-years of camera imagery and net ecosystem exchange measurements from 17 towers spanning three plant functional types (deciduous broadleaf forest, evergreen needleleaf forest, and grassland/crops) to derive color indices and estimate gross primary productivity (GPP). GPP was strongly correlated with greenness derived from camera imagery in all three plant functional types. Specifically, the beginning of the photosynthetic period in deciduous broadleaf forest and grassland/crops and the end of the photosynthetic period in grassland/crops were both correlated with changes in greenness; changes in redness were correlated with the end of the photosynthetic period in deciduous broadleaf forest. However, it was not possible to accurately identify the beginning or ending of the photosynthetic period using camera greenness in evergreen needleleaf forest. At deciduous broadleaf sites, anomalies in integrated greenness and total GPP were significantly correlated up to 60 days after the mean onset date for the start of spring. More generally, results from this work demonstrate that digital repeat photography can be used to quantify both the duration of the photosynthetically active period as well as total GPP in deciduous broadleaf forest and grassland/crops, but that new and different approaches are required before comparable results can be achieved in evergreen needleleaf forest.

Introduction

Climate change impacts on vegetation phenology have been widely documented across a range of biomes and plant functional types (Richardson et al. 2013). In particular, long-term records of leaf and flower phenology in temperate and boreal forest indicate that spring onset is occurring earlier (Aono and Kazui 2008, Miller-Rushing and Primack 2008, Thompson and Clark 2008, Linkosalo et al. 2009), and more generally, that growing seasons are becoming longer on decadal to millennial scales (Menzel 2000). Studies using satellite remote sensing have documented trends toward longer growing seasons over large regions in mid- and high-latitude ecosystems of the Northern Hemisphere (Myneni et al. 1997, Zhang et al. 2007, Jeong et al. 2011, Xu et al. 2013). At lower latitudes, warmer temperatures have led to earlier spring phenology and longer growing seasons in mediterranean ecosystems (Penuelas et al. 2002, Gordo and Sanz 2010), while desert plant

communities have experienced shifts in species composition in response to changes in the timing of winter precipitation (Kimball et al. 2010).

While a large number of studies have identified widespread patterns of change, the impacts of changes in phenology on ecosystem function and feedbacks to the climate system remain poorly understood and quantified (Richardson et al. 2013). For example, multisite comparisons show that growing season length is positively correlated with net ecosystem productivity (NEP; Churkina et al. 2005, Baldocchi 2008), but spatial patterns observed across sites are not identical to temporal patterns at individual sites, which are driven primarily by interannual variability in weather (Richardson et al. 2010). Warmer springs and longer growing seasons have been shown to increase annual carbon uptake in boreal deciduous forest (Barr et al. 2004, 2007), mixed temperate forest (Dragoni et al. 2011), and evergreen needleleaf forest (Richardson et al. 2009*b*, 2010). In subalpine forest, on the other hand, longer growing seasons can lead to lower NEP if warmer temperatures (Sacks et al. 2007) or shallower spring snowpacks (Hu et al. 2010) reduce soil moisture sufficiently to create drought conditions. Similarly, drought conditions in grassland can also shorten the growing season length, thereby lowering annual NEP (Flanagan and Adkinson 2011).

Because phenology is a key regulator of ecosystem function, substantial effort has recently been devoted to expanding networks that track seasonal vegetation dynamics (Morisette et al. 2009). Methods to monitor phenology fall into two broad categories: visual observations and remote sensing. Visual observations provide the oldest and longest-running phenology records in existence (e.g., Aono and Kazui 2008), but visual observations are labor intensive to collect, and the spatial extent of observations collected by an individual is inherently limited. Spaceborne remote sensing, which provides synoptic and global views of land surface phenology and its responses to natural climatic variability, helps to address this limitation (Piao et al. 2006, Dragoni and Rahman 2012, Elmore et al. 2012). However, imagery from remote sensing platforms such as the Moderate Resolution Imaging Spectradiometer (MODIS) is often collected at coarse spatial resolutions (250–500 m) that encompass considerable landscape heterogeneity within each pixel. An additional weakness is the relatively low temporal resolution of some space-borne remote sensing instruments. While coarse spatial resolution sensors such as MODIS provide observations with repeat intervals of 1–2 days, moderate spatial resolution sensors such as Landsat provide a revisit frequency of 16 days, a relatively long interval for capturing rapid changes during seasonal transition periods. In both cases, persistent cloud cover can significantly reduce the frequency of usable observations, which can substantially decrease the utility of space-borne remote sensing for observing and characterizing the timing of key phenological transitions.

Digital repeat photography, a form of near-surface remote sensing, provides data at higher temporal frequency and finer spatial scale than satellite remote sensing (Richardson et al. 2009*a*). Specifically, digital repeat photography can provide imagery that is nearly continuous in time, rarely obscured by clouds, and robust to variation in illumination conditions (Sonnentag et al. 2012). Exploiting this, color indices derived from digital repeat photography have been used to characterize the phenology of diverse plant communities and functional types (PFT) including deciduous broadleaf forest (Richardson et al. 2007, Ahrends et al. 2008, Ide and Oguma 2010, Dragoni et al. 2011, Hufkens et al. 2012, Sonnentag et al. 2012), evergreen broadleaf forest (Zhao et al. 2012), evergreen needleleaf forest (Richardson et al. 2009*a*, Ide and Oguma 2010, Bater et al.

2011), desert shrublands (Kurc and Benton 2010), bryophyte communities (Graham et al. 2006) and invasive plants (Sonnentag et al. 2011). Several studies have used these data to evaluate uncertainties in satellite-based phenological monitoring (Graham et al. 2010, Elmore et al. 2012, Hufkens et al. 2012, Klosterman et al. 2014).

Color indices derived from digital repeat photography have also been correlated with canopy photosynthesis in deciduous broadleaf forest (Richardson et al. 2007, 2009*b*, Ahrends et al. 2009, Mizunuma et al. 2012), grasslands (Migliavacca et al. 2011), and desert shrublands (Kurc and Benton 2010). However, each of these studies was limited to one or two sites and it is unclear how well results from these efforts generalize within and across PFTs at regional to continental scales. Further, a large proportion of previous studies have focused on temperate deciduous forest. Not only does the relationship between annual carbon exchange and the length of the carbon uptake period vary substantially across PFTs (e.g., Richardson et al. 2010), but relationships among camera-based color metrics, phenology, and carbon exchange remain under-studied in ecosystems and PFTs outside of deciduous broadleaf forest (Richardson et al. 2013). Hence, there is a need for improved understanding regarding how canopy photosynthesis is linked to canopy phenology across and within PFTs, and by extension, the role of digital repeat photography for studying these relationships.

With these issues in mind, our objective in this study was to perform a systematic analysis of digital repeat photography as a tool for understanding the relationship between canopy phenology and canopy photosynthesis, both within and among multiple PFTs. To this end, the specific questions guiding this study were:

1. Can camera-derived color indices be used to monitor the seasonality of GPP within and across multiple PFTs?
2. How does the relationship between canopy phenology and GPP vary within and across PFTs?
3. What is the relationship between dynamics in greenness measured from digital camera imagery and key phenophase transitions in different PFTs?
4. Can interannual variation in annual GPP be estimated using camera-derived color indices?

To address these questions, we used data from the PhenoCam network of co-located cameras and eddy covariance towers to assess the relationship between canopy phenology and the seasonality of photosynthesis. Our study, conducted across a range of PFTs, provides the most comprehensive analysis of canopy development and photosynthesis using digital repeat photography to date, and provides useful new understanding regarding the ability of camera-derived color indices to track the seasonality of GPP across space and time.

Methods

Study sites

The study spanned 13 geographically distinct research sites, including 17 flux towers in total (Table 1; Appendix A). We used all possible sites that were members of both the PhenoCam[22] and the AmeriFlux[23] or Canadian Carbon Program[24] networks. In addition, we included four towers, managed by the University of Illinois (UI), that were not members of either network. Each site was dominated by one of three PFTs: deciduous broadleaf forest (DBF), evergreen needleleaf forest (ENF), and grassland/crops (GRS; Table 1). The Groundhog site in Ontario is most accurately described as mixed ENF/DBF; here, we group it with ENF sites because conifer species are dominant. Together, measurements from these sites comprised 59 site-years of concurrent flux and camera data, with 26, 11, and 22 site-years in DBF, ENF, and GRS PFTs, respectively. Most sites had 2–5 years of data. One notable exception, however, is the ARM site in Oklahoma, where data were collected nearly continuously from 2003 to 2011. One of the UI sites featured a crop rotation from maize to soybean in the second year (out of two), which caused significant changes in the magnitude of carbon fluxes. To address this, we treat the two site-years (2009 vs. 2010) as separate sites: UI Maize and UI Soy.

Table 1. Summary of camera/eddy covariance sites used in this study, arranged by plant functional type (PFT; see *Methods*).

Site	PFT	Latitude (°)	Longitude (°)	Altitude (m)	Years	Camera	Citation
Bartlett	DBF	44.0646	−71.2881	268	2006–2012	Axis 211	Richardson et al. (2007)
Harvard	DBF	42.5378	−72.1715	340	2008–2011	StarDot NetCam SC	Urbanski et al. (2007)
Missouri Ozarks	DBF	38.7441	−92.2000	219	2007–2008	Olympus D-360L	Yang et al. (2010)
Morgan Monroe	DBF	39.3231	−86.4131	275	2009–2010	StarDot NetCam SC	Schmid et al. (2000)
U Mich Bio 1	DBF	45.5598	−84.7090	225	2008–2011	StarDot NetCam SC	Nave et al. (2011)
U Mich Bio 2	DBF	45.5598	−84.7138	230	2009–2011	StarDot NetCam SC	Curtis et al. (2002)
Chibougamou	ENF	49.6924	−74.3420	380	2008–2010	StarDot NetCam SC	Bergeron et al. (2007)
Groundhog	ENF/DBF	48.2174	−82.1555	350	2008–2011	StarDot NetCam SC	McCaughey et al. (2006)
Howland	ENF	45.2041	−68.7403	80	2010–2012	Stardot NetCam SC	Hollinger et al. (1999)
Niwot	ENF	40.0328	−105.5470	3055	2008–2011	Canon VB-C10R	Sacks et al. (2007)
Wind River	ENF	45.8213	−121.9521	371	2011	StarDot NetCam SC	Wharton et al. (2012)
ARM Oklahoma	GRS	36.6970	−97.4888	316	2003–2011	Nikon Coolpix 990	Torn et al. (2010)
UI Maize/Soy	GRS	40.0628	−88.1961	314	2009–2010	Axis 211M	Zeri et al. (2011)
UI Miscanthus	GRS	40.0628	−88.1984	314	2009–2010	Axis 211M	Zeri et al. (2011)
UI Prairie	GRS	40.0637	−88.1973	314	2009–2010	Axis 211M	Zeri et al. (2011)
UI Switchgrass	GRS	40.0637	−88.1973	314	2009–2010	Axis 211M	Zeri et al. (2011)
Vaira	GRS	38.4133	−120.9506	129	2009–2010	D-Link DCS-900	Baldocchi et al. (2004)

Note: DBF = broadleaf deciduous forest, ENF = evergreen needleleaf forest, GRS = grassland/crops.

Digital repeat photography

On each eddy covariance tower, the digital camera was installed in a fixed position, with a view across the top of the canopy. Cameras were pointed north to minimize shadows and lens flare, enclosed in commercial waterproof housings, and inclined up to 20° below horizontal. Most cameras collected photos, which were saved in 24-bit JPEG format, at 30–60 minute intervals, 12–24 hours a day. Exceptions include Bartlett (10–20 minute intervals, 1200–1400) and ARM Oklahoma (one midday photo). Half of the towers used StarDot NetCam XL or SC cameras (StarDot Technologies, Buena Park, California, USA), while the other sites used cameras from a variety of manufacturers (Table 1). To minimize the impact of variation in scene illumination (e.g., clouds and aerosols), auto white/color balance was turned off, and exposure adjustment for each camera was set to automatic mode. Note, however, that Vaira was an exception in this regard. To correct for variability

induced by auto color balancing at this site, we used a gray reference panel in the camera field of view (e.g., Jacobs et al. 2009).

Images were either archived by the site investigator or automatically transferred to the PhenoCam server via file transfer protocol (FTP). Time series were first visually inspected for camera shifts and changes in field of view. Noting these changes, we processed the image archives to extract regions of interest (ROI) that encompassed all portions of the full canopy within the foreground (Fig. 1). At Vaira, the ROI was restricted to the grass portion of the image, excluding distant oak trees from analysis. To quantify canopy greenness, we calculated the green chromatic coordinate (GCC), which is widely used to monitor canopy development and identify phenological phase changes (Richardson et al. 2007, Ahrends et al. 2009, Sonnentag et al. 2012, Zhao et al. 2012)

$$GCC = \frac{DN_G}{DN_R + DN_G + DN_B} \qquad (1)$$

where DN is the digital number and R, G, and B denote the red, green and blue channels, respectively. For completeness, we also calculated the Excess Green (ExG) index

$$ExG = 2DN_G - (DN_R + DN_B) \qquad (2)$$

which has been shown to be less noisy than GCC in some coniferous canopies (Sonnentag et al. 2012). To characterize canopy coloration in fall, the red chromatic coordinate (RCC) was calculated using the same form as Eq. 1, substituting DN_R in the numerator.

Figure 1

Open in figure viewer
PowerPoint

Examples of webcam photographs, representing the three plant functional types: (a) Harvard (deciduous broadleaf forest); (b) Chibougamau (evergreen needleleaf forest); and (c) UI Miscanthus (grassland). Polygons indicate the Region of Interest for extracting image greenness.

Following Sonnentag et al. (2012), we calculated the 90th percentile of GCC, ExG, and RCC values for three-day moving windows, yielding up to 122 observations each year. Only photos taken during daylight hours (0600–1800 local time) were included, and any images with underexposed ROIs (which we defined as <15% color saturation, or DN < 39, in any band) were excluded. We did not exclude photos due to poor weather conditions or snow, as the 90th percentile filter successfully removed these (Sonnentag et al. 2012). To eliminate any residual noise we removed GCC or ExG values that exceeded ±2 standard deviations of the mean within 27-day windows. To account for changes in camera settings or shifts in camera fields of view, GCC, RCC, and ExG values

were manually screened and rescaled (as needed) to preserve a smooth and continuous time series at each site.

We used nonlinear least squares regression to fit logistic functions to GCC, RCC, and ExG time series, which were then used to estimate phenophase transition dates from DBF and GRS sites (e.g., Fisher and Mustard 2007, Richardson et al. 2009*a*). For GRS sites, we used separate logistic functions in spring (s) and fall (f)

$$\mathrm{GCC}(t) = a_s + \frac{b_s}{1 + e^{(c_s - d_s t)}} \qquad (3a)$$

$$\mathrm{GCC}(t) = a_f + \frac{b_f}{1 + e^{(c_f + d_f t)}} \qquad (3b)$$

where t is the day of year and the remaining terms are empirically estimated coefficients. For DBF sites, we used the modified logistic function presented by Elmore et al. (2012), which includes an additional parameter (a_2) that accounts for "summer greendown" that is widely observed in DBF greenness time series (Keenan et al. 2014)

$$\mathrm{GCC}(t) = a_1 + (b - a_2 \times t)\left(\frac{1}{1 + e^{(c_s - d_s t)}} - \frac{1}{1 + e^{(c_f - d_f t)}}\right). \qquad (4)$$

Note that in Eq. 4, $a_1 + b$ denotes the early-summer maximum GCC, while the minimum summer GCC value preceding fall coloring is given by $(b - a_2 \times t)$. Coefficients in Eqs. 3 and 4were estimated using the Levenberg-Marquardt method.

Following a widely used remote sensing approach (e.g., Zhang et al. 2003), phenophase transitions were determined by calculating local minima and maxima in the curvature change rate of Eqs. 3 and 4. In spring, maxima correspond to dates of leaf unfolding (start of spring) and maximum greenness (end of spring). In autumn, the onset of fall coloring (start of senescence) and leaf abscission (end of fall) correspond to the timing of minima. The midpoints of each season, middle of spring and middle of fall, were identified using the local minimum and maximum, respectively. We also tested one additional method to estimate the end of fall in DBF sites based on the timing of maximum fall coloring (Richardson et al. 2009*a*), which was determined using the date of the maximum RCC value in the second half of the growing season.

Early analysis indicated that the logistic function provided a poor representation of GCC dynamics at many ENF sites; a separate method was needed to explore links between GCC and GPP seasonality in evergreen sites. Hence, we calculated splines along GCC curves and examined correlations between dates at which a range of GCC thresholds (5–75% of seasonal amplitude, in 5% intervals) were reached, and dates at which a similar range of GPP thresholds were reached.

Eddy covariance data

To assess the ability of camera-based indices to capture seasonal dynamics in carbon fluxes, we compared color indices with estimates of GPP derived from eddy covariance measurements.

To do this we used 30-minute non-gap-filled net ecosystem exchange (NEE) data to estimate GPP, except at the Harvard Forest and Morgan Monroe sites, where only hourly data were available. NEE was partitioned into GPP (micromoles of CO_2 per square meter per second) using the Q_{10} method (Raich and Schlesinger 1992)

$$\mathrm{GPP} = \mathrm{NEE} - R_{\mathrm{eco}} = \mathrm{NEE} - R_{\mathrm{ref}} \times Q_{10}^{(T-T_{\mathrm{ref}})/10} \qquad (5)$$

where R_{ref} is a scaling parameter, Q_{10} is the temperature sensitivity of ecosystem respiration (R_{eco}), and T_{ref} (=10°) is the base temperature where $R_{eco} = R_{ref}$. Friction velocity (u_*) filtering was used to remove nocturnal NEE measurements when there was insufficient turbulence using site-specific u_* values. The Q_{10} function was estimated independently for every site-year, yielding 30-minute estimates of R_{eco} and GPP. When available, we compared our GPP estimates with estimates provided by site investigators. Results from this comparison showed that the estimates were in close agreement (mean R^2 = 0.95; range: 0.91–0.98).

To make the GPP data comparable to the camera-based color indices, we calculated the mean daily-integrated GPP (grams of carbon per square meter per day) across the three-day periods over which the camera data were processed. In addition, we also calculated mean daytime instantaneous flux rates (calculated across all daytime hours, defined as photosynthetic photon flux density (PPFD) ≥ 5 $\mu mol \cdot m^{-2} \cdot s^{-1}$), as well as estimates of the light-saturated rate of photosynthesis (A_{max}, measured as micromoles of CO_2 per square meter per day), which was derived by fitting a Michaelis-Menten light response function to the high-frequency (hourly or half-hourly) flux measurements. The use of these alternative metrics did not change our interpretation (see *Results*). To allow comparison at annual time scales, we calculated annual GPP sums, using the same Q_{10} method as above, but including gap-filled NEE. When gap-filled NEE data were not provided by site investigators, we used an online tool that implements standardized gap filling methods (Reichstein et al. 2005).[25]

To evaluate GCC as a predictor of photosynthesis, daily GPP was regressed against three-day GCC for each tower site. We also regressed the mean daytime instantaneous flux rate (GPP_{30}; averaged over equivalent three-day periods) against GCC, which allowed us to assess this relationship independent of day length. Goodness-of-fit was based on the coefficient of determination (R^2), calculated using linear and quadratic functions at a significance level of 0.05.

A key goal of this analysis was to assess how well dynamics in GCC capture changes in photosynthetic activity corresponding to phenological transitions. For example, one question we examined was, “Does start of spring, estimated by GCC, correspond to the first day of photosynthesis (GPP > 0 g $C \cdot m^{-2} \cdot d^{-1}$) in spring?” To compare relative photosynthetic capacity across sites, we fit smoothing splines to the daily GPP time series for each of the six DBF sites and calculated the percentage of maximum annual flux (maximum daily GPP within a given year = 100%) at 1% intervals along the estimated splines. These data were then pooled, providing a composite DBF data set of 19 site-years. Using phenophase transition dates (start of spring, middle of spring, middle of fall, end of fall) extracted from the GCC and RCC time series, we performed geometric mean regression between camera-derived dates and a range of flux amplitudes (1–90%). Goodness-of-fit was evaluated using the coefficient of determination and the slope of the regression. Bias was quantified using the mean deviation,

and accuracy was evaluated using the root mean square deviation (RMSD) between transition dates estimated from GCC data and transition dates estimated from GPP data.

To explore these relationships at the GRS sites, we pooled data from the four UI sites and performed a parallel analysis. The ARM site in Oklahoma was excluded because both the flux data and the camera data included mixtures of differing phenological patterns associated with multiple crop cycles. We also excluded the Vaira site because it is characterized by asynchronous seasonality (winter active vs. summer active elsewhere) relative to the rest of the sites in our analysis of transition dates. To compare the timing of maximum greenness ($GCC_{90\%}$) and carbon flux ($GPP_{90\%}$), we determined the dates when each metric reached 90% of the maximum annual value at each site using only complete site-years.

Because the rates of spring increase and fall decrease in daily GPP or GCC can vary between years (see Richardson et al. 2010), dates corresponding to the start and end of the growing season may not fully characterize patterns of interannual variability in phenology. To assess this, we tested the hypothesis that during the spring or fall transition periods time-integrated GCC values provide more information about anomalies in GPP than start-of-season or end-of-season dates estimated from GCC time series. To do this, we first re-scaled the GCC and GPP data to account for differences across sites in the magnitude of carbon fluxes and canopy greenness. This provided normalized time series of daily GPP and GCC, both on a scale from 0 to 1. We then fit splines to the normalized GPP and GCC values over 60 day-periods following the earliest start of spring and preceding the latest end of fall, and calculated the integral under each spline curve using numerical approximation. These integrals were then converted to anomalies relative to each site-level mean and used to calculate linear correlations between integrated GCC anomalies and integrated GPP anomalies. To determine whether integrated GCC values provide greater explanatory power than discrete dates such as the start of spring, we compared these results with linear correlations between phenophase transition date anomalies and integrated GPP anomalies. Lastly, we tested whether spring and fall greenness anomalies were correlated with integrated annual GPP anomalies via multiple linear regression, using spring and fall normalized integrated GCC anomalies as independent variables and annual GPP anomalies as the response variable.

Results

Canopy development and photosynthesis; patterns among plant functional types

Time series of GCC and daily GPP (Fig. 2; Appendix B) demonstrate broadly consistent relationships within each of the three PFTs, with some notable exceptions. DBF and GRS sites exhibited clear seasonality in both GCC and GPP, with high values during the photosynthetically active season and low values during the inactive season. GRS sites exhibited shorter but well-defined growing seasons compared to those in DBF (Fig. 2c). In ENF sites, the annual cycle in GCC was roughly sinusoidal, with a relatively short period of minimum values in winter (Fig. 2b). Relationships between GCC and GPP in both the active and dormant seasons were phase-shifted, with spring increases in GCC preceding those in GPP, and autumn decreases in GCC lagging behind GPP.

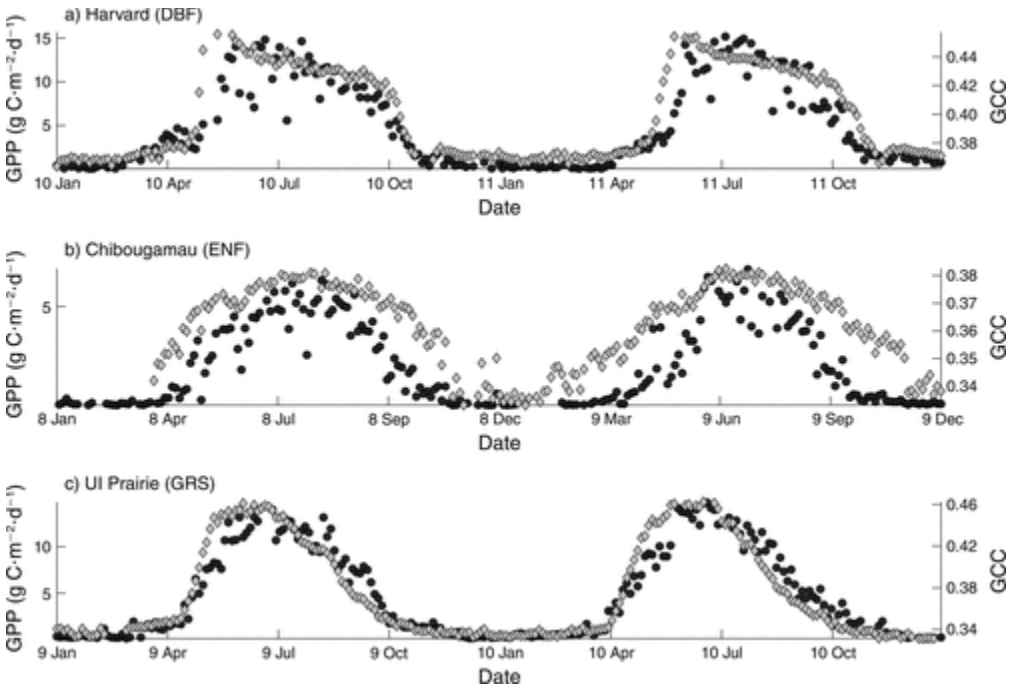

Figure 2

Open in figure viewer
PowerPoint

Time series of daily GPP (black circles, g C·m^{-2}·d^{-1}) and GCC (green chromatic coordinate, gray diamonds) for (a) deciduous broadleaf forest (DBF); (b) evergreen needleleaf forest (ENF); and (c) grassland/crops (GRS). Two characteristic years of data are featured in each subplot. See *Methods* for acronyms.

We also noted distinct differences among the PFTs with regard to the amplitude and range of GCC values. In DBF and GRS, GCC time series were characterized by low values (0.33–0.36) during the winter and high values (0.40–0.50) in peak growing season (Table 1; Appendix B). In contrast, the dynamic range of ENF was much smaller (e.g., seasonal amplitude was 0.04 GCC units for Chibougamau vs. 0.08 GCC units for Harvard; Fig. 2b and 2a, respectively). The smallest range was observed for Wind River, where GCC values varied by just 0.03 throughout the year. There was also a wide range in GPP among PFTs owing to differences in ecosystem productivity arising from factors such as species composition, leaf area, and local climate. Across all sites and PFTs, daily GPP values showed strong seasonal patterns, but there was substantial day-to-day variation caused by changes in short-term environmental conditions (e.g., clouds, vapor pressure deficits, and soil moisture) that limit short-term productivity, and by extension, decrease correlation between GPP and GCC on short (i.e., hours to days) timescales.

Canopy development and photosynthesis; patterns within plant functional types

DBF sites exhibited two primary modes of variation in GCC during the photosynthetically active season. First, over the course of two or three weeks in late spring, GCC tended to exhibit a distinct late-spring “green peak” that was not observed in either ENF or GRS. Second, following this peak, GCC tended to gradually decline over roughly three months, leading to a decrease in GCC of ∼30% relative to the seasonal amplitude. At the onset of leaf coloration, GCC tended to decrease rapidly, leading into the annual winter minimum. Daily GPP, by contrast, increased more slowly throughout the spring, reaching its maximum value 2–4 weeks after the GCC

peak. And, whereas GCC remained high during the summer months, daily GPP tended to decline almost immediately after its peak, well in advance of the fall decline in GCC.

As we noted previously, daily GPP exhibited substantial day-to-day variability in all PFTs. At the Missouri Ozarks site in 2007, however, daily GPP decreased sharply in July, nearly two months before the autumn decrease in GCC, likely in response to moisture stress (Yang et al. 2010). Otherwise, covariance between daily GPP and GCC for DBF sites was generally strong overall (R^2 = 0.50–0.79; Table 2; Fig. 3a; Appendix C) and tended to be linear at lower values of GCC. At higher values of GCC, however, there was little or no relationship between daily GPP and GCC for most DBF sites, which reflects the fact that daily GPP during midsummer is controlled by day-to-day variation in weather that does not affect canopy greenness on short time scales. Correlations between daily GPP and GCC were comparable with those between GCC and GPP_{30} (Table 2), indicating that GCC–GPP relationships are robust and independent of seasonal changes in day length.

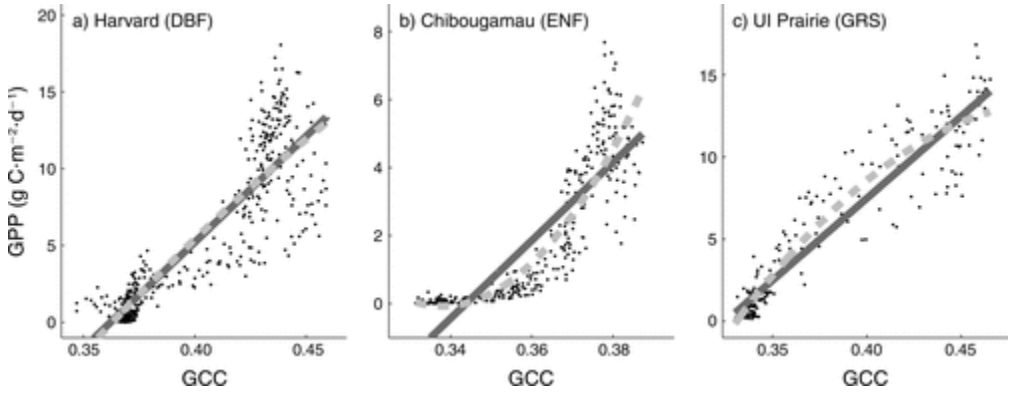

Figure 3

Open in figure viewer
PowerPoint

Scatterplots of daily GPP (g C·m^{-2}·d^{-1}) vs. GCC for (a) deciduous broadleaf forest (DBF); (b) evergreen needleleaf forest (ENF); and (c) grassland (GRS). Linear (dark gray) and quadratic regression lines (dashed light gray) are superimposed (see Table 2 for coefficients of determination). All years of data are featured in each subplot.

Table 2. Coefficients of determination for plant functional types (PFT) linear (R^2) and quadratic regression (R^2_{quad}) of GCC and ExG with daily GPP (GPP_d) and mean 30-minute GPP rate (GPP_{30}).

Site	PFT	GCC-GPP_d		GCC-GPP_{30}		ExG-GPP_d		
		R^2	R^2_{quad}	R^2	R^2_{quad}	R^2	R^2_{quad}	N
Bartlett	DBF	0.782	0.783	0.765	0.773	0.787	0.793	740
Harvard	DBF	0.787	0.809	0.754	0.781	0.710	0.720	428
Missouri Ozarks	DBF	0.498	0.571	0.496	0.551	0.340	0.517	116
Morgan Monroe	DBF	0.629	0.680	0.618	0.706	0.623	0.680	221
U Mich Bio 1	DBF	0.776	0.776	0.794	0.800	0.791	0.792	333
U Mich Bio 2	DBF	0.788	0.819	0.771	0.794	0.415	0.456	356
Chibougamou	ENF	0.723	0.794	0.728	0.792	0.754	0.888	293
Groundhog	ENF/DBF	0.756	0.833	0.754	0.840	0.747	0.789	276
Howland	ENF	0.714	0.735	0.758	0.779	0.769	0.794	310
Niwot	ENF	0.654	0.675	0.707	0.714	0.707	0.761	169
Wind River	ENF	0.527	0.529	0.498	0.547	0.743	0.747	70
ARM Oklahoma	GRS	0.547	0.597	0.648	0.751	0.591	0.629	142
UI Maize	GRS	0.837	0.838	0.874	0.875	0.837	0.837	120
UI Miscanthus	GRS	0.861	0.870	0.872	0.888	0.811	0.828	243
UI Prairie	GRS	0.901	0.916	0.887	0.911	0.892	0.897	238
UI Soy	GRS	0.820	0.822	0.823	0.824	0.786	0.798	120
UI Switchgrass	GRS	0.805	0.815	0.789	0.808	0.749	0.764	243
Vaira	GRS	0.793	0.815	0.759	0.763	0.728	0.815	195

Notes: N is number of observations. In all reported correlations, $P < 0.0001$. See *Methods* for acronyms.

ENF sites were characterized by unique patterns of seasonality in GCC and GPP. Most notably, the period associated with minimum GCC values during winter dormancy was short-lived. At most ENF sites GCC continued to decline into early winter, even when daily GPP was near zero, before rising again in late winter well in advance of the spring onset of photosynthesis. This pattern was not observed at the Wind River site, which was photosynthetically active throughout almost the whole year (Appendix B). Among all ENF sites, the summertime peak in GCC occurred close to the peak in daily GPP. Overall, correlations between daily GPP and GCC were almost as strong (R^2 = 0.53–0.76; Table 2; Appendix C) as those for DBF sites. As with DBF, correlation between GCC and GPP_{30} were comparable with those between GCC and daily GPP (Table 2).

For all but one GRS site, correlations between daily GPP and GCC were high (R^2 = 0.80–0.90; Table 2; Appendix C), and the relationship was linear. Similar to the ENF sites, GCC at GRS sites exhibited a short summer plateau. At the UI Switchgrass and UI Prairie sites, GCC was modestly phase shifted, with GCC leading daily GPP in spring and lagging daily GPP in fall. Covariance between GPP and GCC at the ARM Oklahoma site, where the growing season extends well beyond that at most other sites, was substantially higher between GCC and GPP_{30}than between GCC and daily GPP (Table 2).

For DBF and GRS, relationships between GPP and ExG were similar to those observed for GCC (Table 2). At ENF sites, correlations between ExG and GPP were marginally higher than those between GCC and GPP, but the magnitude of these differences was site specific. At Wind River, in particular, ExG accounted for ~15% more variance in daily GPP than GCC because of the greater stability (less day-to-day noise) in ExG. Similar (but less pronounced) increases were also observed at Chibougamau, Howland, and Niwot.

Camera and flux-based phenophase transitions

Using a combination of greenness (GCC) and redness (RCC) indices, digital repeat photography facilitated accurate determinations of the start and end of the photosynthetic period for DBF and GRS. In ENF sites, however, the lack of a discernible winter baseline prevented accurate estimation of the start and end of canopy photosynthesis. In ENF and GRS, GCC provided a relatively accurate estimation of the date of maximum photosynthesis; however, the relationship in ENF was statistically insignificant. In the section below we elaborate on these themes, discussing four camera-based phenology metrics (start of spring, middle of spring, middle of fall, and end of fall) and their relationship with the seasonality of GPP.

At DBF sites, camera-derived spring and fall phenophase transition dates successfully captured spatiotemporal variability in the beginning and end of the photosynthetic period. Start of spring, estimated using Eq. 4 fit to the GCC time series, was most highly correlated with the day of year corresponding to when flux amplitudes were between 24% and 30% of maximum GPP (R^2 = 0.62; n = 17). Mean deviation (MD) and RMSD between start of spring from GCC and GPP was smallest at 20% and 24% of GPP amplitudes, respectively (Fig. 4a). Results were even stronger (Fig. 4b) for the "middle of spring" (the date on which 50% of the seasonal amplitude in GCC was reached), which corresponded to 30–40% of the spring amplitude in GPP (R^2 = 0.82). In contrast, GCC was a relatively poor predictor of the date of maximum photosynthesis ($GPP_{90\%}$) in DBF sites, with the date of $GCC_{90\%}$ consistently preceding the date of $GPP_{90\%}$ by more than three weeks, on average. Note, however, that the magnitude of this bias was disproportionately influenced by one site-year (Harvard Forest in 2010), in which a late summer increase in GPP delayed the 90% threshold significantly (Fig. 5a).

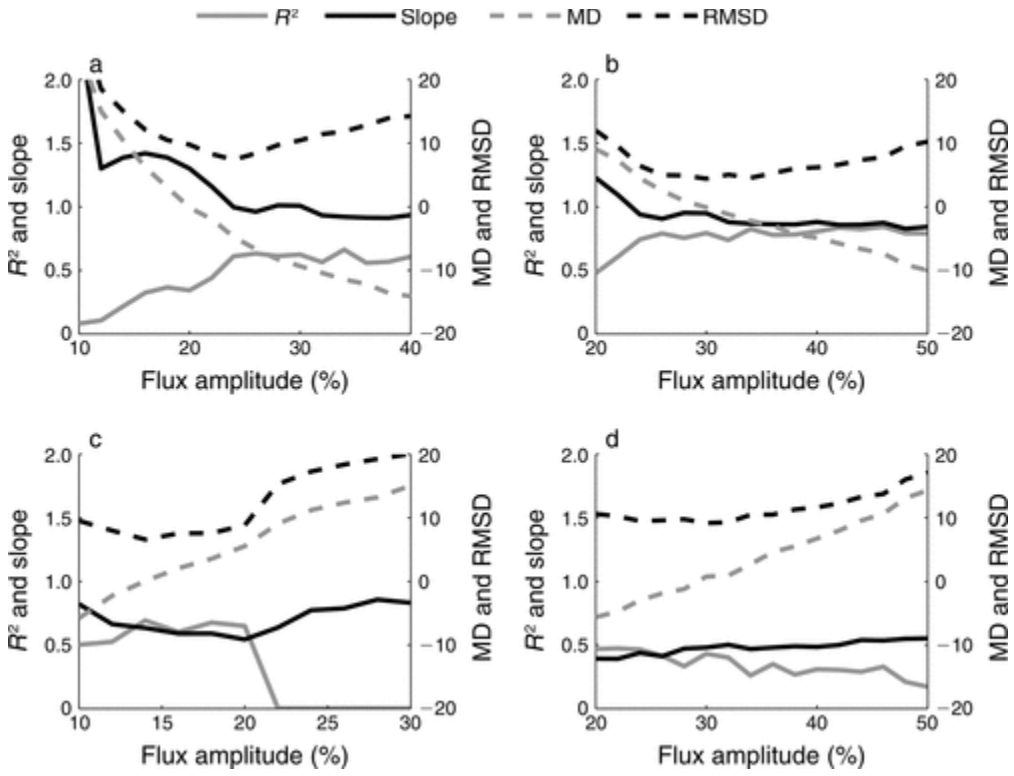

Figure 4

Open in figure viewer
PowerPoint

Four metrics comparing estimates of day of year (see *Methods*) for (a) start of spring, (b) middle of spring, and (d) middle of fall using dates extracted from GCC curve fitting and percentage of maximum

GPP. The plots represent 19 DBF site-years. (c) End of fall camera dates are derived from date of maximum RCC. On left axes, R^2(0.0–1.0) and slope for geometric mean regression. On right axes, mean deviation (MD) and root mean square deviation (RMSD) of estimates; units are days.

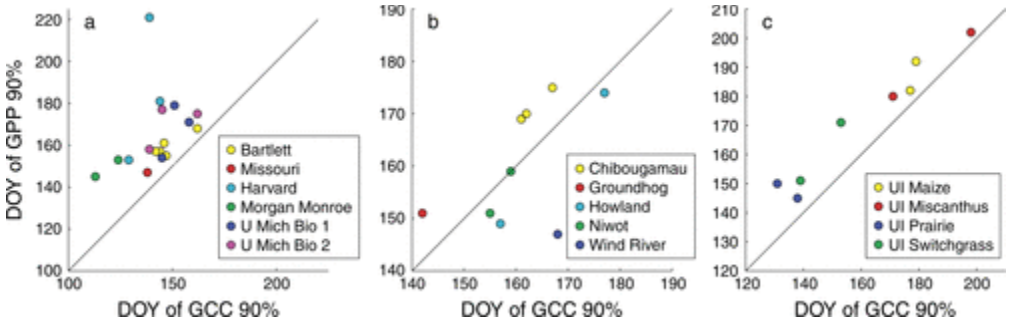

Figure 5

Open in figure viewer
PowerPoint

Comparisons of derived dates (DOY) of maximum greenness and fluxes ($GCC_{90\%}$and $GPP_{90\%}$, respectively) for (a) deciduous broadleaf forest, (b) evergreen needleleaf forest, and (c) grassland/crops sites. DOY 1 is 1 January.

Correlations between the date at which 50% of the seasonal amplitudes in GCC and GPP were reached in fall was relatively weak (R^2 = 0.43; Fig. 4d). Similarly, correspondence between GCC- and GPP-derived end of fall dates was also weak. Canopy redness (RCC), rather than greenness, provided the best indicator of the end of the photosynthetically active period, with the date of peak RCC strongly correlated to the date when GPP amplitude reached 14% (R^2 = 0.69; Fig. 4c).

At GRS sites, GCC provided more information about seasonal dynamics in photosynthesis during spring than in fall. GCC was a good indicator of the beginning of the photosynthetically active period, with high correlation between both the start and middle of spring derived from GCC time series and the date corresponding to a wide range of amplitudes in spring GPP (Fig. 6a, b). Relative to $GPP_{90\%}$, $GCC_{90\%}$ was less biased at GRS sites than at DBF sites (Fig. 5c). Similar to patterns observed in spring, the timing of both the middle and end of fall from GCC showed significant (but lower relative to spring) correlations across a broad range of GPP amplitudes (Fig. 6c).

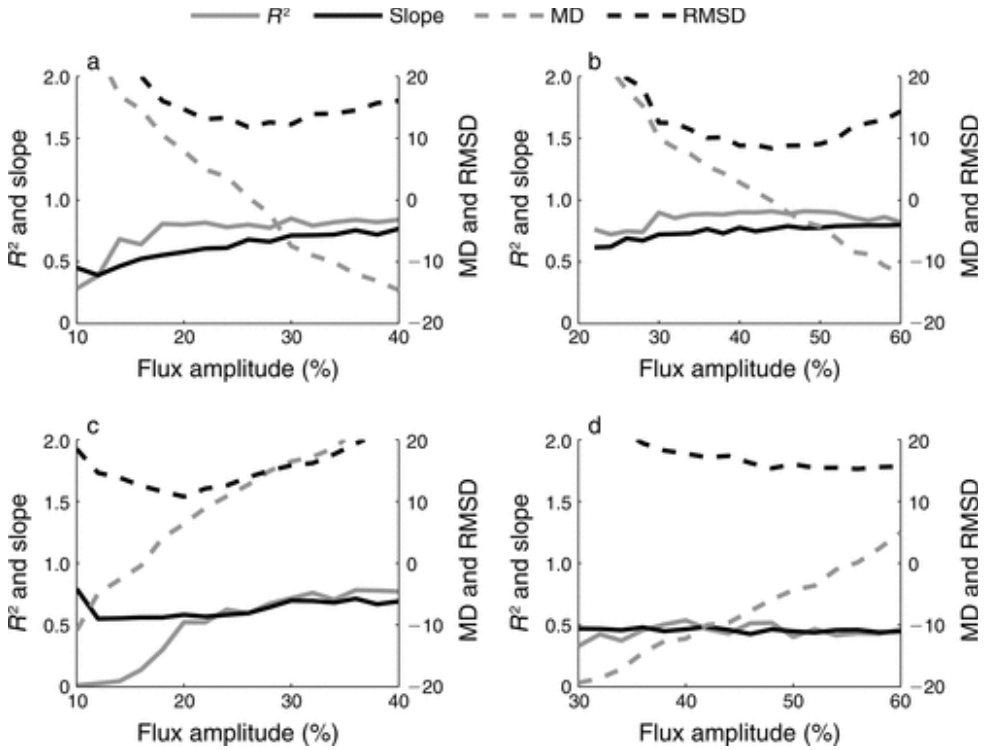

Figure 6

Open in figure viewer
PowerPoint

Four metrics comparing estimates of DOY of (a) start of spring, (b) middle of spring, (c) end of fall, and (d) middle of fall using dates extracted from GCC curve fitting and percentage of maximum GPP. Plots represent 8 GRS site-years. On the left axes, $R^2$and slope for geometric mean regression. On right axes, mean deviation (MD) and root mean square deviation (RMSD) of estimates; units are days. DOY 1 is 1 January.

At ENF sites, GCC typically started to increase prior to the onset of the growing season, when GPP was still zero, and continued to decrease late in the year after GPP had returned to zero. Thus, at both the start and end of the growing season, significant variations in GCC occur that are not associated with dynamics in GPP. Indeed, correlations between the timing of changes in GCC and GPP across a wide range of spring and fall amplitude thresholds (5–75% of seasonal amplitude, in 5% intervals) were statistically insignificant at $P \leq 0.05$. It would appear, therefore, that camera-based GCC time series cannot be used to predict the beginning or end of the photosynthetically active period for ENF sites. It is worth noting, however, that GCC did provide a rough indication of the date of maximum GPP. While the correlation between the dates on which 90% of the spring amplitudes in GCC and GPP were reached was statistically insignificant ($R^2 = 0.32$, $P = 0.11$), the mean bias (across all site-years) was less than one day (0.3 d ± 10 d).

Integrated GCC and GPP

In the final element of our analysis, we investigated whether spring and fall time-integrated sums of daily GCC provide additional or complementary information regarding interannual variation in GPP relative to phenophase transition dates estimated from the GCC time series. To do this, we first focused on the Barlett Forest site and calculated springtime integrated daily GPP and GCC from 2006 to 2012 (Fig. 7). Starting on day

of year (DOY) 115 (selected to precede the earliest observed green-up day, DOY 118), we integrated both GCC and GPP over successively longer time segments at five-day increments (e.g., DOY 115–120, 115–125, etc.). (DOY 1 is 1 January.) Results from this analysis showed that springtime integrated GCC anomalies were strongly and significantly correlated with integrated GPP anomalies for up to 30 days (R^2 = 0.56–0.88; n = 7), by which time cumulative photosynthetic uptake had reached nearly 150 g C/m^2 in some years. GCC and GPP integrals beyond DOY 145 did not show statistically significant correlations. In fall, integrated GCC anomalies computed for time segments spanning 30 days preceding the end of fall (DOY 290) were moderately correlated with corresponding GPP anomalies (R^2 = 0.47; P = 0.09; data not shown). For comparison, start- and middle-of-spring transition dates were modestly correlated with integrated GPP anomalies over the period from DOY 115 to 145 (R^2 = 0.69 and 0.43), while GCC-based middle- and end-of-fall transition dates were highly correlated with time integrals of GPP over the period from DOY 265 to 290 (R^2 = 0.96, 0.70). Thus, at Bartlett, GCC integrals provide more information about flux anomalies than do individual phenological transition dates in the spring, but less information in the fall.

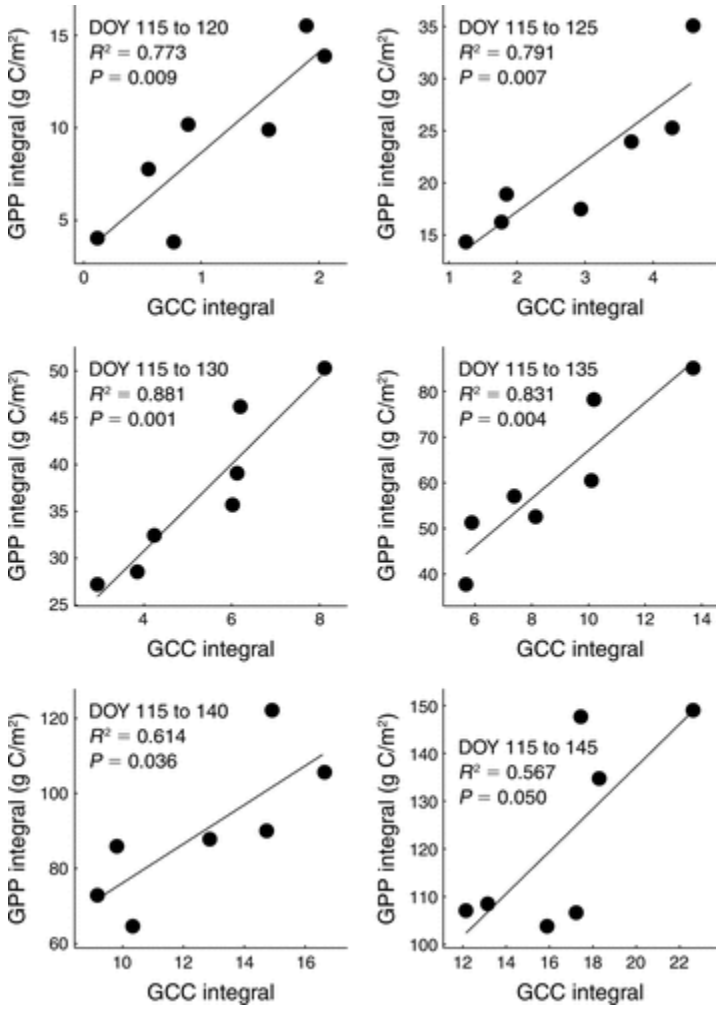

Figure 7

Open in figure viewer
PowerPoint

Regression of GPP integrated sums vs. GCC integrated sums (dimensionless) during the first 30 days following green-up (in 5-day increments) for 2006–2012 at Bartlett.

We then extended this analysis to include all DBF and three of the four Illinois GRS sites (we excluded the UI Maize and UI Soy sites, for which only a single year of data was available). For the DBF sites, we found moderate correlation (as high as $R^2 = 0.49$; $n = 19$ after 30 days) between normalized GCC integral anomalies and normalized GPP integral anomalies up to 60 days after green-up (Fig. 8). Over this period, anomalies of up to 158 g C/m^2 (Harvard), or ~8% of the annual total GPP, were observed. Correlations based on time integrals extending beyond 60 days after the earliest green-up were not statistically significant. In contrast to results at Bartlett Forest, start- and middle-of-spring transition date anomalies were more highly correlated with normalized GPP integral anomalies ($R^2 = 0.71$ and 0.60 at 20 and 30 days, respectively). In fall, correlations between GCC integral anomalies and GPP anomalies were not statistically significant, whereas end-of-fall transition date anomalies were weakly correlated with normalized GPP integral anomalies ($R^2 = 0.30$). Multiple linear regression analysis showed that about half the variance in annual GPP integral anomalies is explained by a combination of spring and fall GCC anomalies ($R^2 = 0.54$). By comparison, a linear model using anomalies in the start-of-spring and end-of-fall transition dates determined from the GCC time series explained less than one-third of the variance in annual GPP integral anomalies ($R^2 = 0.30$). Thus, it is not clear whether integrated GCC provides more information related to interannual variation in GPP than specific transition dates.

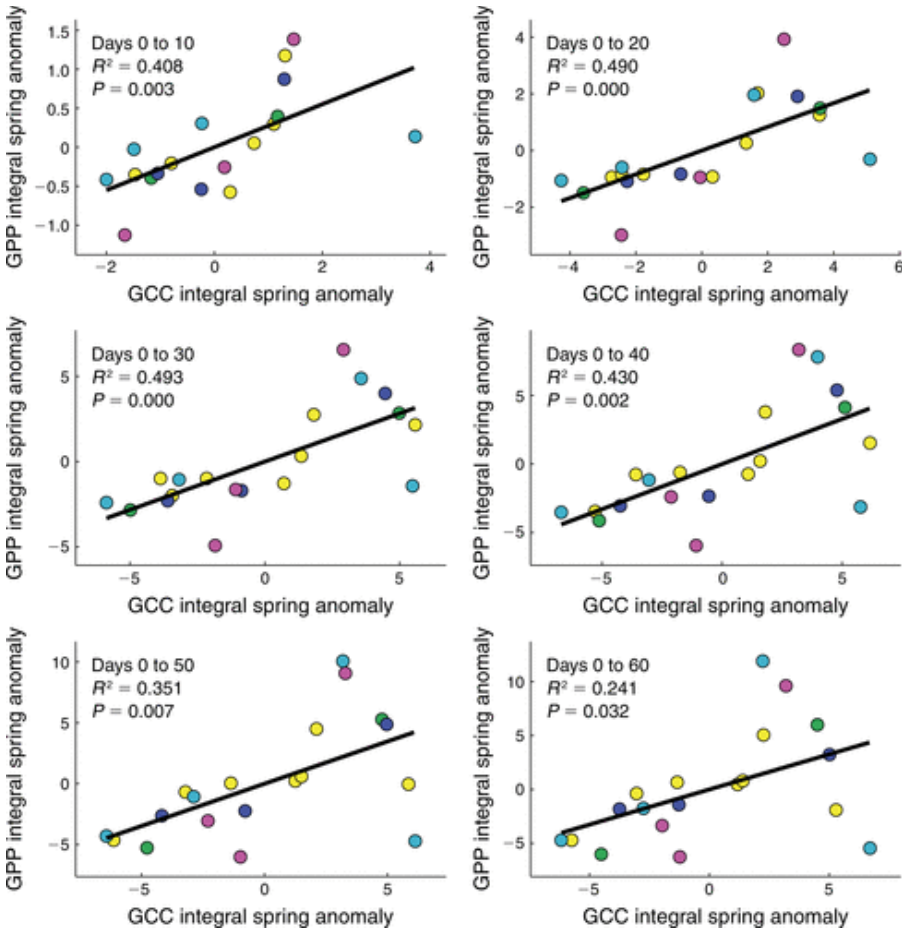

Figure 8

Open in figure viewer
PowerPoint

Regression of GPP integrated sums (dimensionless) vs. GCC integrated sums (dimensionless) during the first 60 days following green-up (shown in 10-day increments) for deciduous broadleaf sites. Legend colors are equivalent to Fig. 5a.

At GRS sites we found strong correlation between normalized GCC anomalies and normalized GPP anomalies up to 60 days after the start of spring (R^2 = 0.97; n = 6; Fig. 9) and during the period 20–50 days preceding the end of the growing season (R^2 = 0.83). While these results are promising, it is important to note that the sample size is small (n = 6) and each tower is represented by only two site-years. As at DBF sites, information related to interannual variation in fall GPP from time-integrated GCC values was comparable to that provided from transition dates, but provided less information related to spring GPP variations. For example, correlation of start-of-spring with spring GPP anomalies was lower than that for GCC anomalies (R^2 = 0.85), while correlation of end-of-fall with fall GPP anomalies (R^2 = 0.81) was equivalent to that of the integrated GCC anomaly.

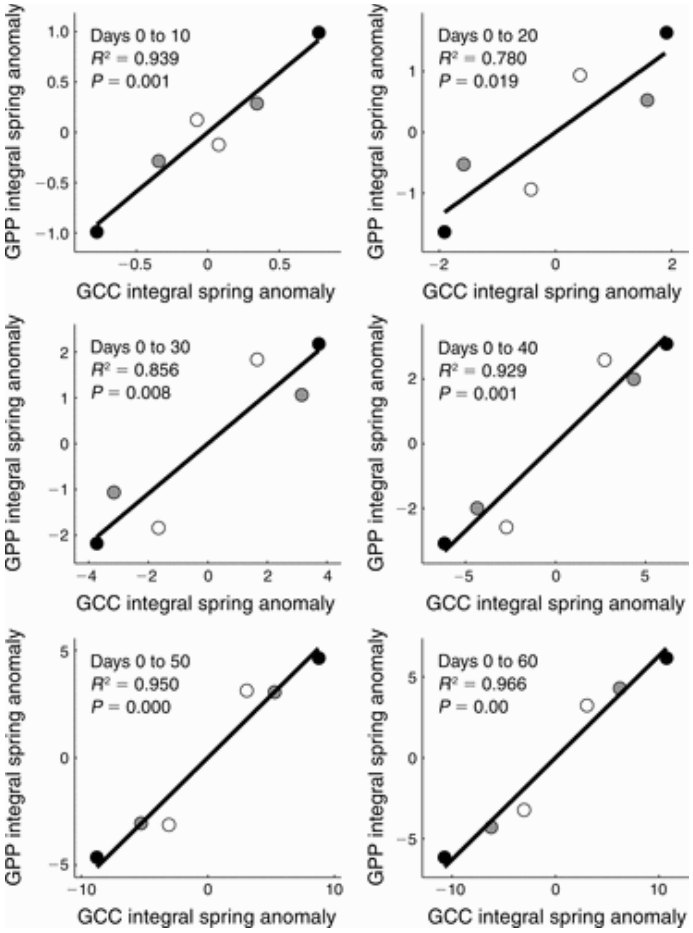

Figure 9

Open in figure viewer
PowerPoint

Regression of normalized GPP integrated sums (dimensionless) vs. GCC integrated sums (dimensionless) during the first 60 days following green-up (in 10-day increments) for the GRS sites, UI Miscanthus (black circles), UI Prairie (white circles) and UI Switchgrass (gray circles).

Discussion

Canopy development and photosynthesis

Results from this study demonstrate that canopy greenness is correlated with rates of photosynthesis in both forest and grassland. Consistent with results from previous studies, canopy greenness and GPP were correlated across DBF sites (Richardson et al. 2007, 2009*a*, Ahrends et al. 2009). For reasons that are unclear, we found a stronger relationship between greenness and photosynthesis in grassland than Migliavacca et al. (2011). At ENF sites, our results are consistent with those obtained by Richardson et al. (2009*a*) and showed moderate to strong correlation between canopy greenness and GPP across all of the sites we examined. This was particularly true for ExG, suggesting that camera-based modeling of GPP in ENF should be based on this index. Specifically, ExG was less sensitive than GCC to variation in illumination conditions. Thus, ExG appears to minimize the impact of shadows, which are prominent and highly variable in conifer canopies.

Our analysis also revealed several limitations of canopy greenness as a predictor of GPP. For example, there was a pronounced peak in GCC at the end of spring in DBF sites (also noted by Mizunuma et al. 2012, Sonnentag et al. 2012) that preceded the peak in GPP by several weeks. Peak GCC is caused by seasonal variation in foliage pigments (e.g., Sims and Gamon 2002) and is accentuated by the oblique viewing angle used by the cameras in this study (Keenan et al. 2014). As a result, $GCC_{90\%}$ tended to occur several weeks before $GPP_{90\%}$. Data from the Missouri Ozarks site also demonstrated limitations of GCC during drought conditions when photosynthesis was reduced by moisture stress, but canopy color was unaffected. As a result, GPP and GCC became decoupled as GPP dropped rapidly while GCC remained high (Appendix B). Even though ENF sites exhibited well-defined seasonality in greenness, GCC was only weakly correlated to GPP at these sites. Conifers undergo seasonal changes in chlorophyll content, with winter minima ~40% lower than summer maxima (Billow et al. 1994, Ottander et al. 1995). Hence, seasonal variation in chlorophyll concentrations at sites with long winters (Chibougamau, Groundhog, Niwot) may be driving observed patterns in canopy greenness, even during the non-photosynthetic period (Fig. 2; Appendix C).

Phenophase transitions and integrated GCC–GPP

Start of spring and end of fall, determined based on GCC and RCC, provided biased estimates for the beginning and cessation of the photosynthetically active period (i.e., GPP > 0 g $C \cdot m^{-2} \cdot d^{-1}$). In deciduous broadleaf forest and grassland/crops sites, the MD and RMSD for the start of spring were lowest for GPP values between 20% and 26% of the spring amplitude, while for end of fall, deviations were lowest for GPP at 14–16% of the fall amplitude. Local maxima in the change in curvature rate, which is used to identify the start of spring and end of fall (Zhang et al. 2003), occurs above wintertime minimum values, when GCC reach ~10% and 90% of the amplitude of Eqs. 3 and 4, respectively. In DBF, an additional source of disagreement between the timing of GCC and GPP is early-season photosynthesis from sub-dominant evergreen trees, which can increase ecosystem GPP well before leaf emergence in deciduous trees.

Garrity et al. (2011) tested 13 metrics of canopy phenology (excluding cameras) and found that no single source provided adequate characterization of the full seasonality of carbon flux phenology. Notably, the beginning of the photosynthetic period was generally well characterized, while the end of the photosynthetic period was poorly characterized, and the timing of maximum GPP was not significantly correlated with any radiometric or remotely sensed variable (Garrity et al. 2011). Although we found similar patterns for DBF sites,

there was relatively close association between $GPP_{90\%}$ and $GCC_{90\%}$ in GRS. Other researchers have found that maximum GCC at DBF sites precedes maximum GPP (Ahrends et al. 2009, Richardson et al. 2009*a*), leaf area index (Keenan et al. 2014), and leaf chlorophyll content (Nagai et al. 2011) by several weeks to two months. Likewise, leaf-level studies indicate long periods (50–80 days) between green-up and maximum photosynthesis (Reich et al. 1991, Bassow and Bazzaz 1998, Morecroft et al. 2003). Thus, it is perhaps not surprising that we found that changes in GCC tend to lead changes in GPP in both spring and autumn in DBF.

A particularly important conclusion from this work is that repeat digital photography not only allows us to identify when photosynthesis begins and ends, but also helps us estimate how much of an impact phenological variability has on seasonal and annual carbon budgets. Using an independent measure of canopy phenology, we showed how changes in the timing of green leaf phenology in the spring and fall affects cumulative photosynthesis. Among DBF sites, we also found significant correlation between combined spring–fall GCC anomalies and anomalies in annual GPP.

Impacts and future work

By examining relationships between camera-derived metrics of greenness and GPP across a large set of sites spanning multiple years and three plant functional types, this research provides an improved foundation for using digital repeat photography to model the impact of phenological dynamics on the carbon cycle of terrestrial ecosystems. Key contributions of this study are (1) demonstration of relatively general relationships between GPP and GCC, and (2) quantification of spatiotemporal variability in canopy development and GPP among and across three major PFTs. More generally, results from this study highlight the role that cameras can play in refining and calibrating phenological subroutines in Earth System models, which vary widely in their representation of green leaf phenology (e.g., Richardson et al. 2012). The Community Land Model, for instance, includes seven PFTs (Bonan et al. 2002), four of which were represented in our study: deciduous broadleaf forest (DBF), coniferous evergreen forest (ENF), grasses (GRS), and crops (GRS). Our study did not include broadleaf evergreen forest, and deciduous and evergreen shrubs, and we are not aware of any studies that have compared camera-based phenology and carbon fluxes in broadleaf evergreen forest (but see Doughty and Goulden 2008 for radiometry-based phenology). However, given the major role of humid tropical forest in the global carbon cycle, there is a clear need for camera-based studies in this biome.

Although our study was focused on canopy-scale phenology, digital repeat photography also has significant potential as a tool for bridging the gap between canopy-to-landscape scale processes and organismal-level observations of leafing and flowering phenology. Digital repeat photography can also play an essential role in scaling organismal- and canopy-level observations to the synoptic scale provided by remote sensing (Hufkens et al. 2012). As networks of spatially referenced online camera imagery rapidly expand (Graham et al. 2010, Sonnentag et al. 2012, Abrams and Pless 2013), opportunities to leverage these networks to monitor and calibrate models of terrestrial phenology are likely to increase. Exploiting this, future work will explore how such camera networks can be used to characterize spatiotemporal variability in phenology and determine the environmental drivers (e.g., temperature, precipitation, photoperiod, snow cover) that regulate canopy development and senescence at regional to continental scales.

Conclusions

In this study, we demonstrate the strengths and limitations of camera-based canopy greenness for monitoring the phenology of photosynthesis in three PFTs: deciduous broadleaf forest, evergreen needleleaf forest and grassland/crops. We encountered key differences among PFTs in the relationship between canopy development, expressed as greenness, and the seasonality of carbon fluxes. These differences were also evident in the detection of discrete phenophase transitions. Canopy greenness proved effective at detecting the beginning and end of the photosynthetically active period in GRS sites. In DBF sites, greenness was effective for detecting the beginning of the photosynthetic period, whereas redness was most effective for detecting the end. A key finding of this study was that integrated GCC was significantly correlated with total GPP during the first 30–60 days following green-up, in both DBF and GRS. In some cases, integrated GCC was a better predictor of summed spring/fall GPP than discrete transitions dates. Further, in DBF there was a moderate correlation between combined spring–fall GCC anomalies and the annual GPP integral anomalies, indicating significant seasonal control of shifts in phenology on ecosystem productivity. Camera data thus provide a valuable and independent means by which ecosystem-scale phenology can be characterized (cf. phenological metrics derived from CO_2 fluxes themselves, as in Richardson et al. 2010). Finally, our results suggest that digital repeat photography may be used to estimate interannual variability in GPP resulting from phenological variability with greater accuracy than many existing ecosystem process models provide (Keenan et al. 2012, Richardson et al. 2012).

Acknowledgments

Development of the PhenoCam network has been supported by the USDA Forest Service's Northeastern States Research Cooperative and the National Science Foundation's Macrosystem Biology Program (award EF-1065029). M. Toomey was partially supported by the U.S. National Park Service Inventory and Monitoring Program and the USA National Phenology Network (grant number G10AP00129 from the United States Geological Survey [USGS]). Research at the Bartlett Experimental Forest tower was supported by the National Science Foundation (grant DEB-1114804), and the USDA Forest Service's Northern Research Station. Research at Howland and Harvard Forest was supported by the Office of Science Biological and Environmental Research (BER), U.S. Department of Energy. Research at ARM Oklahoma was also supported by BER under Contract No. DE-AC02-05CH11231 as part of the Atmospheric Radiation Measurement program and Atmospheric System Research program. Research at the UMBS was supported by BER (project DE-SC0006708) and NSF (grant DEB-0911461). The Groundhog and Chibougamau sites, as parts of the Canadian Carbon Program, received funding from the Canadian Foundation for Climate and Atmospheric Sciences (CFCAS), NSERC, Natural Resources Canada, and Environment Canada. The contents of this paper are solely the responsibility of the authors and do not necessarily represent the official views of NSF or USGS.

- http://phenocam.sr.unh.edu/
- http://ameriflux.ornl.gov/
- http://fluxnet.ornl.gov/site_list/Network/3
- http://www.bgc-jena.mpg.de/~MDIwork/eddyproc/

References

1. Abrams, A., and R. Pless. 2013. Web-accessible geographic integration and calibration of webcams.*Association for Computing Machinery Transactions on Multimedia Computing, Communications, and Applications 9*. http://dx.doi.org/10.1145/2422956.2422964

2. Ahrends, H. E., R. Brugger, R. Stockli, J. Schenk, P. Michna, F. Jeanneret, H. Wanner, and W. Eugster.2008. Quantitative phenological observations of a mixed beech forest in northern Switzerland with digital photography. *Journal of Geophysical Research-Biogeosciences* **113**: G04004.

3. Ahrends, H. E., S. Etzold, W. L. Kutsch, R. Stockli, R. Bruegger, F. Jeanneret, H. Wanner, N. Buchmann, and W. Eugster. 2009. Tree phenology and carbon dioxide fluxes: use of digital photography for process-based interpretation of the ecosystem scale. *Climate Research* **39**: 261–274.

4. Aono, Y., and K. Kazui. 2008. Phenological data series of cherry tree flowering in Kyoto, Japan, and its application to reconstruction of springtime temperatures since the 9th century. *International Journal of Climatology* **28**: 905–914.

5. Baldocchi, D. 2008. 'Breathing' of the terrestrial biosphere: lessons learned from a global network of carbon dioxide flux measurement systems. *Australian Journal of Botany* **56**: 1–26.

6. Baldocchi, D., L. Xu, and N. Kiang. 2004. How plant functional-type, weather, seasonal drought, and soil physical properties alter water and energy fluxes of an oak–grass savanna and an annual grassland. *Agricultural and Forest Meteorology* **123**: 13–39.

7. Barr, A. G., T. A. Black, E. H. Hogg, T. J. Griffis, K. Morgenstern, N. Kijun, A. Theede, and Z. Nesic. 2007.Climatic controls on the carbon and water balances of a boreal aspen forest, 1994–2003. *Global Change Biology* **13**: 561–576.

8. Barr, A. G., T. A. Black, E. H. Hogg, N. Kljun, K. Morgenstern, and Z. Nesic. 2004. Inter-annual variability in the leaf area index of a boreal aspen-hazelnut forest in relation to net ecosystem production. *Agricultural and Forest Meteorology* **126**: 237–255.

9. Bassow, S. L., and F. A. Bazzaz. 1998. How environmental conditions affect canopy leaf-level photosynthesis in four deciduous tree species. *Ecology* **79**: 2660–2675.

10. Bater, C. W., N. C. Coops, M. A. Wulder, S. E. Nielsen, G. McDermid, and G. B. Stenhouse. 2011.Design and installation of a camera network across an elevation gradient for habitat assessment.*Instrumentation Science & Technology* **39**: 231–247.

11. Bergeron, O., H. A. Margolis, T. A. Black, C. Coursolle, A. L. Dunn, A. G. Barr, and S. C. Wofsy. 2007.Comparison of carbon dioxide fluxes over three boreal black spruce forests in Canada. *Global Change Biology* **13**: 89–107.

12. Billow, C., P. Matson, and B. Yoder. 1994. Seasonal biochemical changes in coniferous forest canopies and their response to fertilization. *Tree Physiology* **14**: 563–574.

13. Bonan, G., S. Levis, L. Kergoat, and K. Oleson. 2002. Landscapes as patches of plant functional types: an integrating concept for climate and ecosystem models. *Global Biogeochemical Cycles* 16.

14. Churkina, G., D. Schimel, B. H. Braswell, and X. Xiao. 2005. Spatial analysis of growing season length control over net ecosystem exchange. *Global Change Biology* **11**: 1777–1787.

15. Curtis, P. S., P. J. Hanson, P. Bolstad, C. Barford, J. C. Randolph, H. P. Schmid, and K. B. Wilson. 2002.Biometric and eddy-covariance based estimates of annual carbon storage in five eastern North American deciduous forests. *Agricultural and Forest Meteorology* **113**: 3–19.

16. Doughty, C. E., and M. Goulden. 2008. Seasonal patterns of tropical forest leaf area index and CO_2exchange. *Journal of Geophysical Research* **113**: G00B06.

17. Dragoni, D., and A. F. Rahman. 2012. Trends in fall phenology across the deciduous forest of the Eastern USA. *Agricultural and Forest Meteorology* **157**: 96–105.

18. Dragoni, D., H. P. Schmid, C. A. Wayson, H. Potter, C. S. B. Grimmond, and J. C. Randolph. 2011.Evidence of increased net ecosystem productivity associated with a longer vegetated season in a deciduous forest in south-central Indiana, USA. *Global Change Biology* **17**: 886–897.

19. Elmore, A. J., S. M. Guinn, B. J. Minsley, and A. D. Richardson. 2012. Landscape controls on the timing of spring, fall, and growing season length in mid-Atlantic forest. *Global Change Biology* **18**: 656–674.

20. Fisher, J. I., and J. F. Mustard. 2007. Cross-scalar satellite phenology from ground, Landsat, and MODIS data. *Remote Sensing of Environment* **109**: 261–273.

21. Flanagan, L. B., and A. C. Adkinson. 2011. Interacting controls on productivity in a northern Great Plains grassland and implications for response to ENSO events. *Global Change Biology* **17**: 3293–3311.

22. Garrity, S. R., G. Bohrer, K. D. Maurer, K. L. Mueller, C. S. Vogel, and P. S. Curtis. 2011. A comparison of multiple phenology data sources for estimating seasonal transitions in deciduous forest carbon exchange. *Agricultural and Forest Meteorology* **151**: 1741–1752.

23. Gordo, O., and J. J. Sanz. 2010. Impact of climate change on plant phenology in Mediterranean ecosystems. *Global Change Biology* **16**: 1082–1106.

24. Graham, E. A., M. P. Hamilton, B. D. Mishler, P. W. Rundel, and M. H. Hansen. 2006. Use of a networked digital camera to estimate net CO_2 uptake of a desiccation-tolerant moss. *International Journal of Plant Sciences* **167**: 751–758.

25. Graham, E. A., E. C. Riordan, E. M. Yuen, D. Estrin, and P. W. Rundel. 2010. Public Internet-connected cameras used as a cross-continental ground-based plant phenology monitoring system. *Global Change Biology* **16**: 3014–3023.

26. Hollinger, D. Y., S. M. Goetz, E. A. Davidson, J. T. Lee, K. Tu, and H. T. Valentine. 1999. Seasonal patterns and environmental control of carbon dioxide and water vapour exchange in an ecotonal boreal forest. *Global Change Biology* **5**: 891–902.

27. Hu, J., D. J. P. Moore, S. P. Burns, and R. K. Monson. 2010. Longer growing seasons lead to less carbon sequestration by a subalpine forest. *Global Change Biology* **16**: 771–783.

28. Hufkens, K., M. Friedl, O. Sonnentag, B. H. Braswell, T. Milliman, and A. D. Richardson. 2012. Linking near-surface and satellite remote sensing measurements of deciduous broadleaf forest phenology.*Remote Sensing of Environment* **117**: 307–321.

29. Ide, R., and H. Oguma. 2010. Use of digital cameras for phenological observations. *Ecological Informatics* **5**: 339–347.

30. Jacobs, J., et al . 2009. *The global network of outdoor webcams: properties and applications*. Association for Computing Machinery International Conference on Advances in Geographic Information Systems, 4–6 November 2009. Seattle, Washington, USA.

31. Jeong, S.-J., H. Chang-Hoi, G. Hyeon-Ju, and M. E. Brown. 2011. Phenology shifts at start vs. end of growing season in temperate vegetation over the Northern Hemisphere for the period 1982–2008.*Global Change Biology* **17**: 2385–2399.

32. Keenan, T. F., et al . 2012. Terrestrial biosphere model performance for inter-annual variability of land-atmosphere CO_2 exchange. *Global Change Biology* **18**: 1971–1987.

33. Keenan, T. F., et al . 2014. Tracking forest phenology and seasonal physiology using digital repeat photography: a critical assessment. *Ecological Applications* **24**: 1478–1489.

34. Kimball, S., A. L. Angert, T. E. Huxman, and D. L. Venable. 2010. Contemporary climate change in the Sonoran Desert favors cold-adapted species. *Global Change Biology* **16**: 1555–1565.

35. Klosterman, S. T., K. Hufkens, J. M. Gray, E. Melaas, O. Sonnentag, I. Lavine, L. Mitchell, R. Norman, M. A. Friedl, and A. D. Richardson. 2014. Evaluating remote sensing of deciduous forest phenology at multiple spatial scales using PhenoCam imagery. *Biogeosciences Discussions* **11**: 2305–2342.

36. Kurc, S. A., and L. M. Benton. 2010. Digital image-derived greenness links deep soil moisture to carbon uptake in a creosotebush-dominated shrubland. *Journal of Arid Environments* **74**: 585–594.

37. Linkosalo, T., R. Hakkinen, J. Terhivuo, H. Tuomenvirta, and P. Hari. 2009. The time series of flowering and leaf bud burst of boreal trees (1846–2005) support the direct temperature observations of climatic warming. *Agricultural and Forest Meteorology* **149**: 453–461.

38. McCaughey, J. H., M. R. Pejam, M. A. Arain, and D. A. Cameron. 2006. Carbon dioxide and energy fluxes from a boreal mixedwood forest ecosystem in Ontario, Canada. *Agricultural and Forest Meteorology* **140**: 79–96.

39. Menzel, A. 2000. Trends in phenological phases in Europe between 1951 and 1996. *International Journal of Biometeorology* **44**: 76–81.

40. Migliavacca, M., et al . 2011. Using digital repeat photography and eddy covariance data to model grassland phenology and photosynthetic CO_2 uptake. *Agricultural and Forest Meteorology* **151**: 1325–1337.

41. Miller-Rushing, A. J., and R. Primack. 2008. Global warming and flowering times in Thoreau's Concord: a community perspective. *Ecology* **89**: 332–341.

42. Mizunuma, T., M. Wilkinson, E. Eaton, M. Mencuccini, J. Morison, and J. Grace. 2012. The relationship between carbon dioxide uptake and canopy colour from two camera systems in a deciduous forest in southern England. *Functional Ecology* **27**: 196–207.

43. Morecroft, M. D., V. J. Stokes, and J. I. L. Morison. 2003. Seasonal changes in the photosynthetic capacity of canopy oak (*Quercus robur*) leaves: the impact of slow development on annual carbon uptake. *International Journal Biometeorology* **47**: 221–226.

44. Morisette, J. T., et al . 2009. Tracking the rhythm of the seasons in the face of global change: phenological research in the 21st century. *Frontiers in Ecology and Environment* **7**: 253–260.

45. Myneni, R. B., C. D. Keeling, C. J. Tucker, G. Asrar, and R. R. Nemani. 1997. Increased plant growth in the northern high latitudes from 1981 to 1991. *Nature* **386**: 698–702.

46. Nagai, S., T. Maeda, M. Gamo, H. Muraoka, R. Suzuki, and K. N. Nasahara. 2011. Using digital camera images to detect canopy condition of deciduous broad-leaved trees. *Plant Ecology and Diversity 4*: 79–89.

47. Nave, L. E., et al . 2011. Disturbance and the resilience of coupled carbon and nitrogen cycling in a north temperate forest. *Journal of Geophysical Research* **116**: G04016.

48. Ottander, C., D. Campbell, and G. Oquist. 1995. Seasonal changes in photosystem II organization and pigment composition in *Pinus sylvestris*. *Planta* **197**: 176–183.

49. Penuelas, J., I. Filella, and P. Comes. 2002. Changed plant and animal life cycles from 1952 to 2000 in the Mediterranean region. *Global Change Biology* **8**: 531–544.

50. Piao, S., J. Fang, L. Zhou, P. Ciais, and B. Zhu. 2006. Variations in satellite-derived phenology in China's temperate vegetation. *Global Change Biology* **12**: 672–685.

51. Raich, J. W., and W. H. Schlesinger. 1992. The global carbon dioxide flux in soil respiration and its relationship to climate. *Tellus* **44B**: 81–99.

52. Reich, P. B., M. B. Walters, and D. S. Ellsworth. 1991. Leaf age and season influence the relationships between leaf nitrogen, leaf mass per area and photosynthesis in maple and oak trees. *Plant, Cell and Environment* **14**: 251–259.

53. Reichstein, M., et al . 2005. On the separation of net ecosystem exchange into assimilation and ecosystem respiration: review and improved algorithm. *Global Change Biology* **11**: 1424–1439.

54. Richardson, A. D., B. H. Braswell, D. Y. Hollinger, J. P. Jenkins, and S. V. Ollinger. 2009 *a*. Near-surface remote sensing of spatial and temporal variation in canopy phenology. *Ecological Applications* **19**: 1417–1428.

55. Richardson, A. D., D. Y. Hollinger, D. B. Dail, J. T. Lee, W. Munger, and J. O'Keefe. 2009 *b*. Influence of spring phenology on seasonal and annual carbon balance in two contrasting New England forests.*Tree Physiology* **29**: 321–331.

56. Richardson, A. D., J. P. Jenkins, B. H. Braswell, D. Y. Hollinger, S. V. Ollinger, and M. L. Smith. 2007. Use of digital camera images to track spring green-up in a deciduous broadleaf forest. *Oecologia* **152**: 323–334.

57. Richardson, A. D., T. F. Keenan, M. Migliavacca, Y. Ryu, O. Sonnentag, and M. Toomey. 2013. Climate change, phenology, and phenological control of vegetation feedbacks to the climate system.*Agricultural and Forest Meteorology* **169**: 156–173.

58. Richardson, A. D., et al . 2010. Influence of spring and fall phenological transitions on forest ecosystem productivity. *Philosophical Transactions of the Royal Society* B **365**: 3227–3246.

59. Richardson, A. D., et al . 2012. Terrestrial biosphere models need better representation of vegetation phenology: results from the North American Carbon Program Site Synthesis. *Global Change Biology***18**: 566–584.

60. Sacks, W. J., D. S. Schimel, and R. K. Monson. 2007. Coupling between carbon cycling and climate in a high-elevation, subalpine forest: a model-data fusion analysis. *Oecologia* **151**: 54–68.

61. Schmid, H. P., C. S. B. Grimmond, F. Cropley, B. Offerle, and H. B. Su. 2000. Ecosystem-atmosphere exchange of carbon dioxide over a mixed hardwood forest in the mid-western United States.*Agricultural and Forest Meteorology* **103**: 357–374.

62. Sims, D. A., and J. A. Gamon. 2002. Relationship between leaf pigment content and spectral reflectance across a range of species, leaf structures and developmental stages. *Remote Sensing of Environment* **81**: 337–354.

63. Sonnentag, O., M. Detto, R. Vargas, Y. Ryu, B. R. K. Runkle, M. Kelly, and D. D. Baldocchi. 2011.Tracking the structural and functional development of a perennial pepperweed (*Lepidium latifolium*L.) infestation using a multi-year archive of webcam imagery and eddy covariance measurements.*Agricultural and Forest Meteorology* **151**: 916–926.

64. Sonnentag, O., K. Hufkens, C. Teshera-Sterne, A. M. Young, M. Friedl, B. H. Braswell, T. Milliman, J. O'Keefe, and A. D. Richardson. 2012. Digital repeat photography for phenological research in forest ecosystems. *Agricultural and Forest Meteorology* **152**: 159–177.

65. Thompson, R., and R. M. Clark. 2008. Is spring starting earlier? *Holocene* **18**: 95–104.

66. Torn, M. S., S. C. Biraud, C. J. Still, W. J. Riley, and J. A. Berry. 2010. Seasonal and inter-annual variability in δ_{13}C of net ecosystem carbon exchanges from 2002–2009 in the U.S. Southern Great Plains. *Tellus B* **63B**: 181–195.

67. Urbanski, S., C. Barford, S. Wofsy, C. Kucharik, E. Pyle, J. Budney, K. McKain, D. Fitzjarrald, M. Czikowsky, and J. W. Munger. 2007. Factors controlling CO_2 exchange on timescales from hourly to decadal at Harvard Forest. *Journal of Geophysical Research* **112**: G02020.

68. Wharton, S., M. Falk, K. Bible, M. Schroeder, and K. T. Paw U. 2012. Old-growth CO_2 flux measurements reveal high sensitivity to climate anomalies across seasonal, annual and decadal time scales. *Agricultural and Forest Meteorology* **161**: 1–14.

69. Xu, L., et al . 2013. Temperature and vegetation seasonality diminishment over northern lands.*Nature Climate Change*. http://dx.doi.org/10.1038/nclimate1836

70. Yang, B., et al . 2010. Environmental controls on water use efficiency during severe drought in an Ozark Forest in Missouri, USA. *Global Change Biology* **16**: 2252–2271.

71. Zeri, M., K. Anderson-Teixeira, G. Hickman, M. Masters, E. DeLucia, and C. J. Bernacchi. 2011. Carbon exchange by establishing biofuel crops in Central Illinois. *Agriculture, Ecosystems and Environment* **144**: 319–329.

72. Zhang, X., M. A. Friedl, C. B. Schaaf, A. Strahler, J. C. F. Hodges, F. Gao, B. C. Reed, and A. Huete. 2003.Monitoring vegetation phenology using MODIS. *Remote Sensing of Environment* **84**: 471–475.

73. Zhang, X., D. Tarpley, and J. T. Sullivan. 2007. Diverse responses of vegetation phenology to a warming climate. *Geophysical Research Letters* **34**: L19405.

74. Zhao, J., Y. Zhang, Z. Tan, Q. Song, N. Liang, L. Yu, and J. Zhao. 2012. Using digital cameras for comparative phenological monitoring in an evergreen broad-leaved forest and a seasonal rain forest. *Ecological Informatics* **10**: 65–72.